Structural Descriptors of Zeolitic–Imidazolate Frameworks Are Keys to the Activity of Fe–N–C Catalysts

Vanessa Armel,[†] Sheena Hindocha,[‡] Fabrice Salles,[†] Stephen Bennett,[‡] Deborah Jones,[†] and Frédéric Jaouen*,[†]

[†]Institut Charles Gerhardt Montpellier, Laboratory for Aggregates, Interfaces and Materials for Energy, UMR 5253, CNRS, Université de Montpellier, 34095 Montpellier, France
[‡]Johnson Matthey Technology Centre, Sonning Common, Berkshire RG4 9NH, United Kingdom

ⓢ Supporting Information

ABSTRACT: Active and inexpensive catalysts for oxygen reduction are crucially needed for the widespread development of polymer electrolyte fuel cells and metal–air batteries. While iron–nitrogen–carbon materials pyrolytically prepared from ZIF-8, a specific zeolitic imidazolate framework (ZIF) with sodalite topology, have shown enhanced activities toward oxygen reduction in acidic electrolyte, the rational design of sacrificial metal–organic frameworks toward this application has hitherto remained elusive. Here, we report for the first time that the oxygen reduction activity of Fe–N–C catalysts positively correlates with the cavity size and mass-specific pore volume in pristine ZIFs. The high activity of Fe–N–C materials prepared from ZIF-8 could be rationalized, and another ZIF structure leading to even higher activity was identified. In contrast, the ORR activity is mostly unaffected by the ligand chemistry in pristine ZIFs. These structure–property relationships will help identifying novel sacrificial ZIF or porous metal–organic frameworks leading to even more active Fe–N–C catalysts. The findings are of great interest for a broader application of the class of inexpensive metal–nitrogen–carbon catalysts that have shown promising activity also for the hydrogen evolution (Co–N–C) and carbon dioxide reduction (Fe–N–C and Mn–N–C).
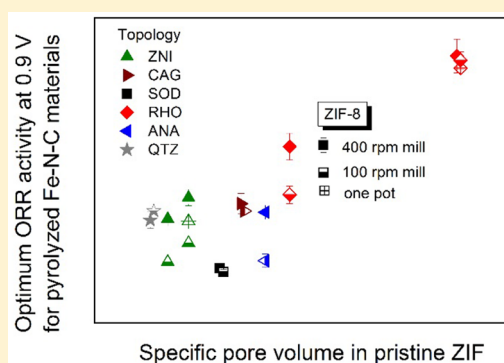
INTRODUCTION

In combination with the production of renewable energy, electrification of the automobile is a leading opportunity for cleaner cities on a local scale and reduced dependence on fossil fuels on a global scale.[1] Rechargeable batteries and H_2/air fuel cells are more efficient than combustion engines and do not release noxious gases and particles. Thus, if electricity and H_2 are produced from renewable energies and water respectively, then operation of battery and fuel cell vehicles would lead to a zero carbon footprint. Battery-driven vehicles will however likely remain restricted to commuting usage due to intrinsic material properties limiting the energy density of batteries and the rate at which they may be safely recharged.[2] In contrast, the most recent proton exchange membrane fuel cell (PEMFC) stacks and H_2 storage systems match the long driving range and short refueling time currently offered by fossil-fueled combustion engines. While fuel cell vehicles have been recently launched on the market, the current PEMFC automotive stacks still suffer from economic drawbacks, with a significant cost fraction originating from the large amount of platinum needed to activate the oxygen reduction reaction (ORR) at the cathode. Recently, important achievements for the ORR electrocatalysis have been reported for platinum nanostructures alloyed with transition or rare-earth metals[3−6] and for advanced Fe–N–C cathodes with initial power performance rivaling Pt-based cathodes.[7−10] In the long term, the successful replacement of Pt by earth-abundant elements would offer key advantages such as lowered cost, decreased fuel crossover effects, and increased tolerance to H_2-fuel or airborne impurities. In particular, Fe–N–C catalysts prepared via the pyrolysis of sacrificial metal–organic frameworks (MOFs) have set the state-of-the-art ORR activity and initial power performance of this class of materials since 2011.[7,10−14] The rational design of MOFs toward the synthesis of highly active Fe–N–C catalysts has however hitherto remained elusive, with ZIF-8 still prevailing thus far.[7,10] ZIF-8 comprises Zn(II) cations and 2-methylimidazolate ligands crystallized in sodalite topology. MOF structures exclusively based on Fe or Co cations did not result in highly active Fe(Co)–N–C catalysts due to excessive contents of Fe or Co.[15−17] Regarding this aspect, ZIF-67 is instructive, being isostructural to ZIF-8, the only difference being the nature of the metal ion, Co(II) in ZIF-67 and Zn(II) in ZIF-8. Pyrolyzing ZIF-67 (26.4 wt % Co before pyrolysis) in inert atmosphere resulted in a Co–N–C catalyst with moderate ORR activity compared to that of catalysts prepared from ZIF-8 functionalized with 0.5−2 wt % Fe.[7,17] The intrinsic advantages of MOF structures based on

Table 1. Chemical and Structural Properties of Pristine ZIFs[a]

formula, name	topology	Zn/C ratio	N/C ratio	cavity size (Å)	specific pore volume (cm³ g⁻¹)	specific surface area (m² g⁻¹)
Zn(Im) (mIm), ZIF-61	zni	0.143	0.571	1.16	0.21	0
Zn(eIm)₂	qtz	0.100	0.400	1.50	0.17	0
Zn(Im)₂	zni	0.167	0.670	3.16	0.27	0
Zn(bzIm)₂, ZIF-7	sod	0.071	0.286	3.50	0.37	180
Zn(Im)₂, ZIF-4	cag	0.167	0.670	4.76	0.43	0
Zn(eIm)₂, ZIF-14	ana	0.100	0.400	5.00	0.49	1160
Zn(mIm)₂, ZIF-8	sod	0.125	0.500	11.10	0.66	1756
Zn(bzIm)₂, ZIF-11	rho	0.071	0.286	13.80	0.56	1732
Zn(eIm)₂	rho	0.100	0.400	18.00	1.05	2100

[a]ZIF materials are ranked according to increasing cavity size. The cavity size, specific pore volume, and specific surface area are derived from simulation-assisted structural determination (see Methods section). Zero specific surface area means the molecular probe (N_2) is smaller than the aperture size and cannot enter the ZIF structure.

Zn(II) cations are (i) the low boiling temperature of Zn allowing its removal during pyrolysis and (ii) the inability of Zn to catalyze graphitization. Excessive Fe or Co contents result during pyrolysis in the formation of reduced metallic or metal-carbide structures that catalyze the graphitization of carbon.[15,16] Carbons that are too graphitic are disadvantageous for metal–N–C catalysts due to low specific area and reduced number of CoN_4 and FeN_4 active moieties.[17,18]

While MOFs exclusively based on ferrous or cobaltous cations result in metal contents well above the optimum,[19,20] novel bimetallic Zn/Fe or Zn/Co ZIFs with sodalite topology have been synthesized.[21–23] The Zn/Fe and Zn/Co atomic ratios in those bimetallic ZIFs closely followed the salt concentrations in the crystallizing solution. Core–shell structures comprising a core based on a Zn(II) ZIF and a shell of a Co(II)- or Fe(II)-based ZIF have also been reported, allowing a low content of Fe or Co in catalyst precursors.[24] A third route has involved various one-pot approaches, whereby Fe or Co salts or complexes are not incorporated at nodes of the crystalline MOF structure but are believed to partially fill the large cavities of the host MOF.[11,13,25,26] Finally, porous organic polymers of polymerized Fe porphyrins have been used as sacrificial precursors comprising a suitable Fe amount (ca. 2 wt %) given the high mass of the porphyrinic ligands.[27]

Due to the recent introduction of MOFs as sacrificial precursors toward the synthesis of metal–N–C catalysts, structure–property relationships between the structure of the parent MOFs and the ORR activity of the resulting metal–N–C catalysts have not yet been clearly identified, impeding a rational selection of MOFs.[13,26,28] Comparatively, the investigation of structure–property relationships between sacrificial MOFs and carbon materials derived from them has been investigated in more depth, focusing on the specific area and morphological aspects of the resulting carbons.[29,30] Lim et al. found a positive correlation between zinc content in pristine MOFs and the specific surface area of the resulting carbon materials.[29] These MOFs were based on Zn(II) cations and various carboxylate ligands or biligands. This correlation was tentatively explained by the evaporation of Zn during pyrolysis, with the metal acting as a foaming agent. They however found no correlation between the specific surface areas of pristine MOFs and the specific areas of the derived carbon materials.[29] Some nonporous MOFs (i.e., those lacking pores accessible to the N_2 molecular probe) even lead to highly porous carbon materials. The significant formation of volatile species from pristine MOFs during pyrolysis and the complete rearrangement of a minor fraction of carbon atoms from MOFs into a more or less graphitic structure can deeply modify the microporous structure during pyrolysis, explaining how non-porous MOFs may lead to porous carbons. This initial comprehension of structure–structure relationships between MOFs and MOF-derived carbons is of interest for metal–N–C catalysts. For the latter, both the fate of carbon and nitrogen atoms during pyrolysis and the fate of Fe or Co ions are important.[18,31]

With the objective of identifying structure–property relationships between the chemistry and/or structure of pristine ZIFs and in contrast the ORR activity of pyrolyzed Fe–N–C catalysts, we systematically compared nine ZIF structures. They were selected to cover a vast range of structural and chemical characteristics of ZIFs. Through the systematic investigation of the ORR activity of ZIF-derived Fe–N–C catalysts and structural characterization of pristine ZIFs and catalyst precursors before pyrolysis, several structure–property relationships have been identified for the first time in this work. The cavity size and mass-specific pore volume in pristine ZIFs are shown to be key descriptors for the preparation of highly active Fe–N–C catalysts.

■ RESULTS AND DISCUSSION

Pristine ZIF Structure and Chemistry. We synthesized nine Zn-based ZIF structures (see the Methods section), with robust synthesis readily available at the multigram scale and covering a broad range of topologies and coordination chemistries (Table 1). All structures are based on ZnN_4 coordination tetrahedra involving different ligands, namely, imidazolate (Im), 2-methylimidazolate (mIm), 2-ethylimidazolate (eIm), and benzimidazolate (bzIm). Their structure was verified via the match between experimental X-ray diffraction (XRD) patterns and patterns calculated for the targeted structures (Figure S1). The structural and chemical properties of these nine ZIFs are reported in Table 1. While some structures are identified with a widely accepted abbreviation or number, such as ZIF-7 or ZIF-8, others are not. The latter are uniquely referred to in this work by their stoichiometric metal–ligand formula and topology (e.g., Zn(eIm)₂ qtz). The Zn/C and N/C ratios reported in Table 1 are derived from the known Zn/ligand stoichiometry in each ZIF. While the cavity sizes in most ZIFs investigated here have previously been estimated, the estimations made by different groups involved different calculation methods and assumptions.[32–35] In order to free ourselves from a possible bias due to different calculation approaches, all ZIF structures were reoptimized with a single calculation approach (see the Methods section). The cavity size
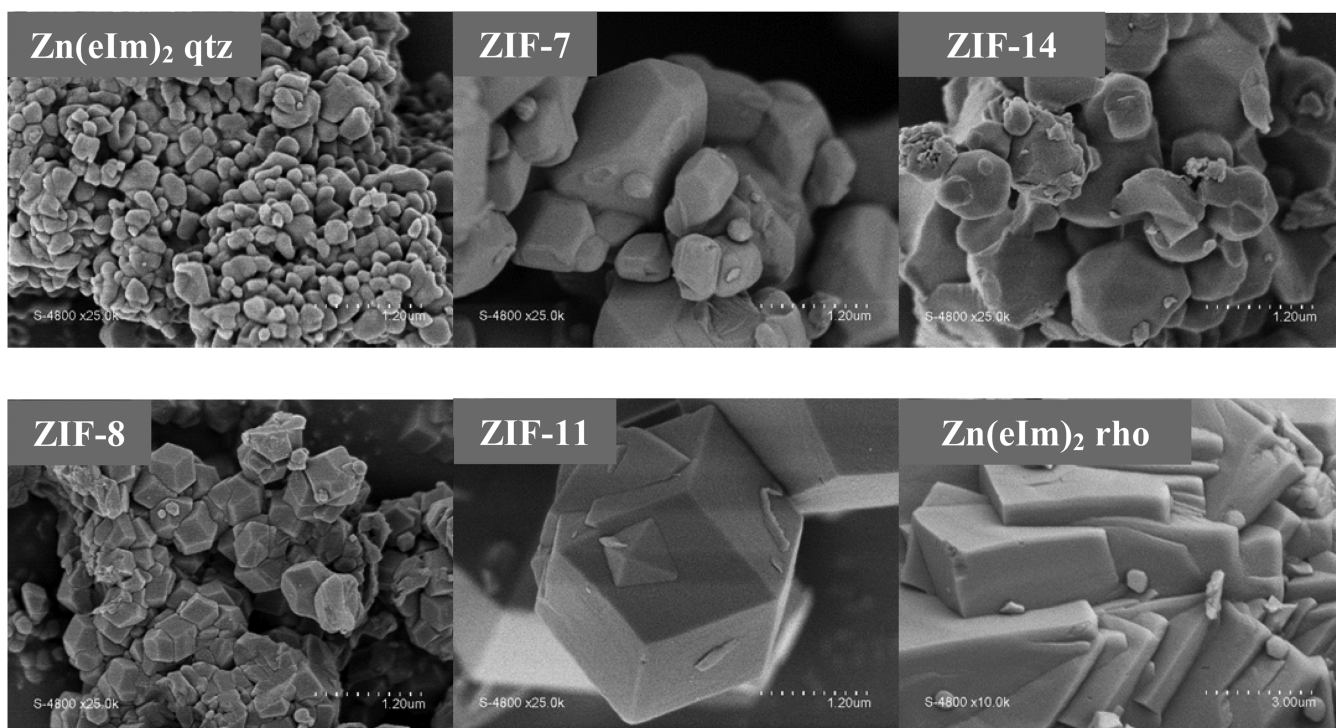
Figure 1. Characteristic SEM micrographs for some of the pristine ZIFs investigated in this work. The scale bar is 1.20 μm for all micrographs, except for Zn(eIm)$_2$ rho (3.00 μm).

was obtained from the pore size distribution functions, shown in Figure S2. The mass-specific pore volume and specific surface area in the optimized ZIF structures were also accessible via computational methods (Table 1). ZIF structures whose aperture is smaller than the molecular probe (N_2) have a closed porosity and therefore no accessible internal surface area (last column in Table 1).

All ZIFs were also characterized with scanning electron microscopy (SEM) to investigate their macroscopic morphology. Figure 1 presents characteristic SEM images for selected ZIFs, while Figures S3 and S4 present a characteristic micrograph for each ZIF and at two different magnifications. SEM micrographs reveal major differences in the particle or crystal size of the various ZIFs. Except for Zn(eIm)$_2$ rho, all ZIFs show a fairly unimodal particle or crystal size distribution. The single-crystal nature of the apparent objects with well-defined facets is obvious for ZIF-61, ZIF-8, ZIF-11, ZIF-4, and Zn(eIm)$_2$ rho, and is less so for Zn(eIm)$_2$ qtz, Zn(Im)$_2$ zni, ZIF-7, and ZIF-14 (Figures S3 and S4). The Zn(eIm)$_2$ rho material shows a clear bimodal crystal size distribution, centered at about 1−2 μm and then at 30−50 μm. All peaks of its experimental XRD pattern could however be assigned to the calculated Zn(eIm)$_2$ rho structure, demonstrating the purity of the product (Figure S1).

Structure−Activity Relationships for Catalysts Derived from Amorphous Precursors. A first series of catalyst precursors and catalysts was then prepared via the planetary milling of fixed amounts of dry powders of Fe(II) acetate, 1,10-phenanthroline (phen), and a given ZIF (Methods). The milling speed employed was 400 rpm, as previously used in most of our investigations involving ZIF-8 as a sacrificial MOF.[7,12,31] All catalyst precursors were then pyrolyzed for 15 min at a set temperature in flowing NH_3. For each ZIF, we explored the effect of pyrolysis temperature in the range of 900

to 1000 °C, by steps of 50 °C. Pyrolysis at 1050 °C was also investigated for catalysts whose activity increased after raising the pyrolysis temperature from 950 to 1000 °C. The temperature of 900 °C is the lower end of interest, due to the boiling point of zinc being 907 °C. Below 900 °C, the amount of residual Zn in the catalysts increases, and ZIFs only partially transform into carbon materials, both leading to low ORR activity.[7] After pyrolysis at 900 °C, the catalysts showed Zn contents between 0.01 and 4.61 wt %, depending on the pristine ZIF, then 0.01−2.14 wt % Zn after pyrolysis at 950 °C and only 0.01−0.66 wt % Zn after pyrolysis at 1000 °C (Table S1). The removal of Zn during pyrolysis is therefore mostly independent of the ZIF structure and mostly dependent on the pyrolysis temperature. The ORR activity of all catalysts was investigated in a single-cell PEMFC. The polarization curves of some Fe−N−C cathode catalysts (loading 1 mg$_{\text{Fe−N−C}}$ cm^{-2}) are shown in Figure 2, spanning the whole range of ORR activities observed in this study after pyrolysis-temperature optimization for each ZIF. The current density at 0.9 V ranges from ca.1 to almost 6 mA cm^{-2}, with Zn(eIm)$_2$ rho resulting in the best catalyst of this study with an activity higher than that of the optimized catalyst derived from ZIF-8. The latter, while not showing the highest current density at 0.9 V, however resulted in a cathode with better mass-transport characteristics leading to higher current density at low potential (i.e., at $E < 0.77$ V, Figure 2). The cathode performance at low potential is the outcome of numerous factors, including ORR activity and Tafel slope, O_2 diffusion properties, electrode hydrophobicity, and electron and proton conductivity. Many of these properties, O_2 diffusion in particular, are impacted by the Fe−N−C macroscopic morphology. The latter is in turn much affected by the macroscopic morphology of pristine ZIFs, which differs significantly among the various ZIFs investigated in this work (Figures 1, S3, and S4). SEM images of selected Fe−N−C
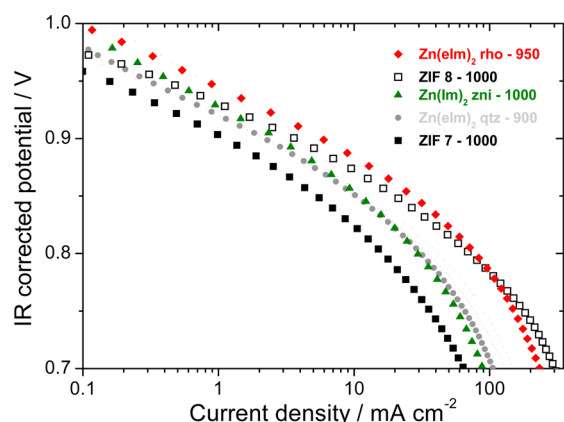
Figure 2. PEMFC polarization curves presented as Tafel plots for selected Fe−N−C catalysts of the first series (400 rpm milling rate). The 3−4 digit numbers in the legend represent the pyrolysis temperature in NH_3, optimized for each ZIF. The anode and cathode catalyst loadings were 0.5 mg_{Pt} cm^{-2} and 1.0 mg_{FeNC} cm^{-2}, respectively. O_2 and H_2 were fully humidified, and the pressure was 1 bar gauge on each side. The cell temperature was 80 °C.

catalysts from the first series are shown in Figure S5. Comparison of Figures 1 and S5 show that a macroscopic templating effect of ZIF crystals into Fe−N−C catalytic particles indeed occurred. The synthesis of a particular ZIF

material can be adapted to minimize its crystal size, which improves the mass-transport characteristics of the corresponding Fe−N−C catalyst while leaving its ORR activity unaffected, as recently shown by us.[36] Different ZIF-8 materials with average crystal sizes ranging from 1600 down to 100 nm were synthesized and resulted in a set of Fe−N−C catalysts with similar ORR activities but improved mass-transport properties when starting with nano-ZIF-8.[36] We therefore decided to focus in this work on understanding why different ZIF topologies (microstructures) resulted in Fe−N−C catalysts with different ORR activities at 0.9 V. The underlying factors governing ORR activity are expected to be microscopic rather than macroscopic, since the activity is per definition not affected by reactant transports to/from the active sites.

Inspired by a previous study having reported a correlation between the specific Brunauer−Emmett−Teller (BET) area of carbons derived from various MOFs and the Zn/C ratio in pristine MOFs,[29] a possible correlation between the ORR activity of Fe−N−C catalysts and the Zn/C ratio in pristine ZIFs was investigated. Figure 3a clearly shows that no such trend is observed for the first series of Fe−N−C catalysts, even when considering only the ORR activity measured after an optimized pyrolysis temperature (filled symbols). The large range of optimized activities that are observed starting with various ZIFs having similar Zn/C ratio (e.g., at Zn/C = 0.09−0.1) indicates that Zn/C is not a key descriptor of ZIFs for
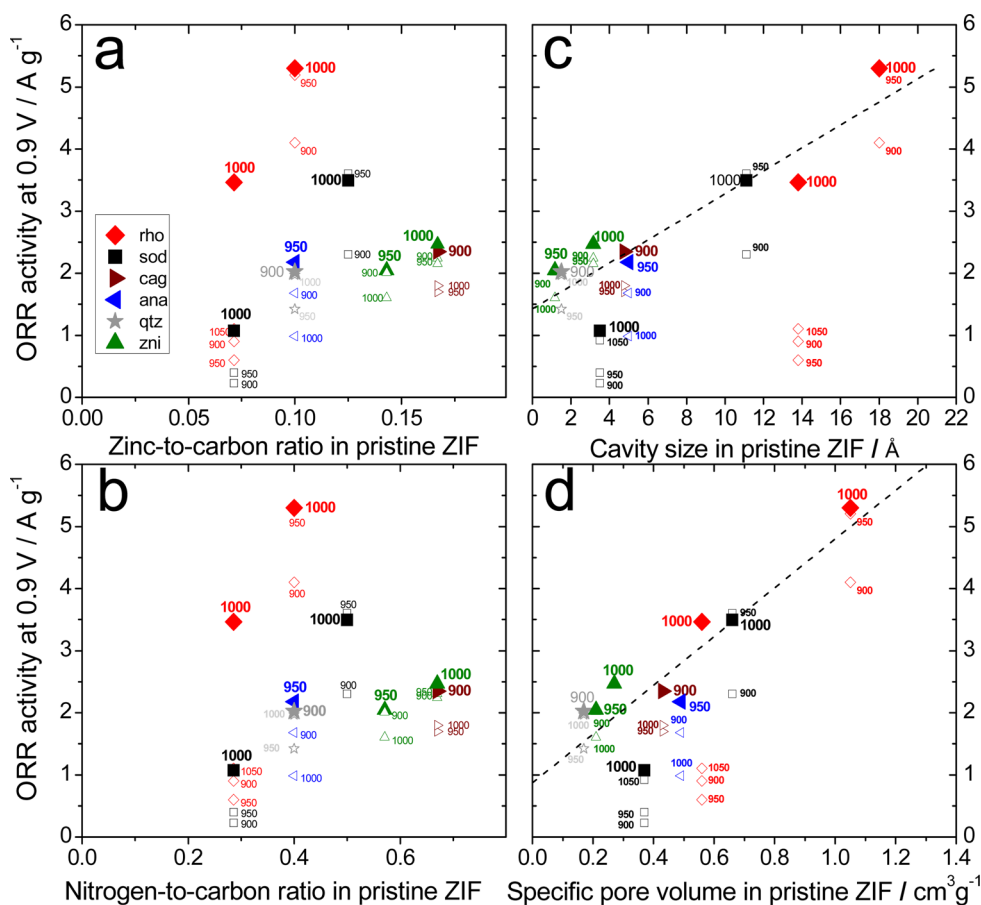

Figure 3. Attempted relationship between the ORR activity of Fe−N−C catalysts and the composition or structure of pristine ZIFs. (a) Lack of correlation between ORR activity and Zn/C ratio in pristine ZIFs, (b) lack of correlation between ORR activity and N/C ratio in pristine ZIFs, (c) correlation between ORR activity and the cavity size of pristine ZIFs, and (d) correlation between ORR activity and the specific pore volume of pristine ZIFs. Dotted lines represent linear fittings obtained from the activity data at optimum temperature (filled symbols).

preparing Fe−N−C catalysts (Figure 3a). Similarly, the N/C ratio is not a key descriptor of ZIFs for the present Fe−N−C catalysts (Figure 3b). Thus, the chemical composition of Zn-based ZIFs does not explain the activity variations among the present Fe−N−C catalysts. This becomes even more obvious when considering three ZIFs comprising the ligand eIm, namely, Zn(eIm)$_2$ qtz, ZIF-14 and Zn(eIm)$_2$ rho (Table 1). They result in a common Zn/C ratio of 0.1, but in very different ORR activities for the Fe−N−C materials (Figure 3a, filled symbols corresponding to Zn/C = 0.1). Since these three ZIFs as well as other ZIF subsets based on identical ligands (see Table 1, two ZIFs with Im, two ZIFs with bzIm) resulted in Fe−N−C catalysts with different ORR activities, we then considered the structure of pristine ZIFs as a possible key descriptor. Considering that Zn(II) cations and a given imidazolate ligand may crystallize in two or more topologies depending on crystallization conditions, structural descriptors may explain why several ZIFs with identical building units may lead to Fe−N−C materials with different activities. The first structural parameter of pristine ZIFs that we consider is the cavity size, a key parameter for gas adsorption and separation as well as catalytic applications of pristine MOFs. Figure 3c shows a preliminary positive correlation between the cavity size of pristine ZIFs and the ORR activity of the first series of Fe−N−C catalysts, in particular when considering the optimum ORR activity measured for each ZIF-derived catalyst (filled symbols). The dotted line in Figure 3c represents the fit obtained between the optimized ORR activity for each ZIF-derived catalyst and the cavity size in pristine ZIFs. As mentioned earlier, the possible importance of cavity size in pristine ZIFs toward the formation of highly active Fe−N−C catalysts had first been hinted at by Banerjee's group[26] but was observed for materials with poor ORR activity. While the cavity size is one structural descriptor, the mass-specific pore volume of ZIFs may be a more general descriptor of ZIFs having nonspherical cavity shapes. A second positive correlation is in fact observed between the specific pore volume of pristine ZIFs and the ORR activity of Fe−N−C materials (Figure 3d). The dotted line again represents the fit obtained from the temperature-optimized activities (filled symbols). The main difference between trends seen in Figure 3c,d pertains to the position of ZIF-11 (red diamonds), situated on the right side of ZIF-8 in Figure 3c but on its left side in Figure 3d. This is caused by the bzIm ligand resulting in a larger cavity size in ZIF-11 versus ZIF-8 but in lower mass-specific volume due to the higher molecular mass of bzIm versus mIm (Table 1). The linear correlation between increased ORR activity of Fe−N−C materials (ca.1 to 6 Ag^{1-}) and increasing specific pore volume in pristine ZIFs (0.17 to 1.32 cm^{3}g^{-1}) is convincing for the optimized catalysts (filled symbols), especially taking into account that the pyrolysis temperature was increased by large steps of 50 °C. While not being the sole parameters defining the maximum ORR activity that may be reached with Fe−N−C catalysts derived from a given ZIF, the cavity size and specific pore volume of pristine ZIFs seem to be key structural features for the synthesis of highly active Fe−N−C materials.

The temperature effect in the range 900−1050 °C (fixed pyrolysis duration of 15 min in NH$_3$) is generally not great among this set of catalysts, except for Fe−N−C materials derived from ZIF-11 (red diamonds, corresponding to a specific pore volume 0.56 cm^{3}g^{-1} in Figure 3d). Figure S6 shows XRD patterns for Fe−N−C catalysts derived from ZIF-7, ZIF-61, ZIF-14, and ZIF-11 after pyrolysis at 900−1000 °C. It can be

seen that the pristine ZIF materials transformed into more or less graphitized carbon structures. The 2θ position of the 002 diffraction line of pure graphite is 26.3°. The apparent peak position is 25.6−25.9° for this first series of catalysts, indicating an increased d_{002} lattice spacing relative to graphite. The amorphous character of the carbon matrix is also revealed through the asymmetry of the 002 diffraction line, particularly visible for catalysts derived from ZIF-11 (Figure S6d). Fitting strategies of the asymmetric 002 diffraction line for amorphous carbons comprising a graphitic and an amorphous phase have involved two symmetric peaks, with the peak with lower 2θ position assigned to the amorphous phase.[37] The latter is important in Fe−N−C catalysts in order to host a large number of FeN$_4$ moieties, the most active sites in such materials.[31] For a given ZIF, the pyrolysis temperature leading to the highest ORR activity often corresponds to the highest possible temperature that does not lead to the massive formation of Fe$_3$C and α-Fe structures (Figure S6). An increased amount of Fe$_3$C and α-Fe is paralleled by the narrowing of the 002 graphite peak (i.e., by increasing graphitization). The latter is known to be intimately related to the destruction of FeN$_4$ moieties during pyrolysis.[18]

Based on the preliminary observation of a relationship between structural parameters of pristine ZIFs (cavity size, specific pore volume) and the ORR activity of Fe−N−C catalysts derived from them (Figure 3c,d), we then verified if the catalyst precursors were still characterized by the crystalline structures of pristine ZIFs after the milling step. Figure 4a
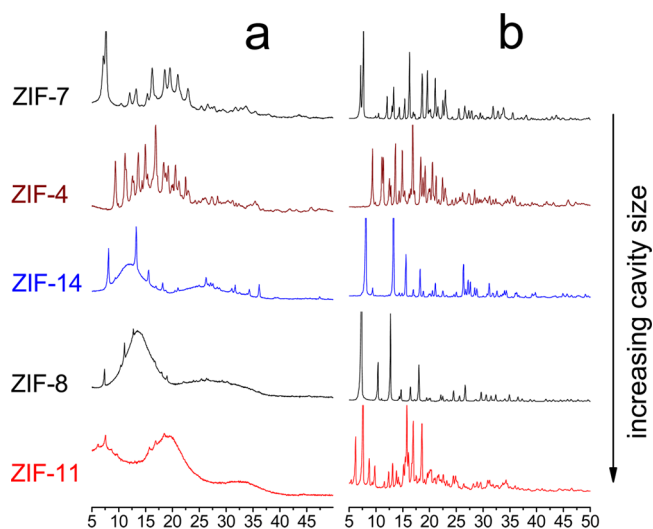

Figure 4. Effect of cavity size and ball milling rate on the crystallinity of catalyst precursors. Dry powders of ZIF (800 mg), phen (200 mg), and FeAc (31 mg) were ball milled at (a) 400 rpm and (b) 100 rpm. The figure is organized so that the cavity size in the pristine ZIF structures increases from top to bottom.

shows the XRD patterns for selected catalyst precursors, obtained by milling ferrous acetate, phen and each pristine ZIF at 400 rpm (see Methods). Except for Zn(eIm)$_2$ qtz, all catalyst precursors showed XRD patterns assigned to partially or fully amorphized ZIF structures (Figures 4a and S7). The catalyst precursors selected to construct Figure 4 encompass the whole range of degrees of amorphization, from a significantly retained crystalline order for catalyst precursors based on ZIF-7 and ZIF-4 to advanced amorphization for those prepared with ZIF-14 and ZIF-8 and complete amorphization for that derived
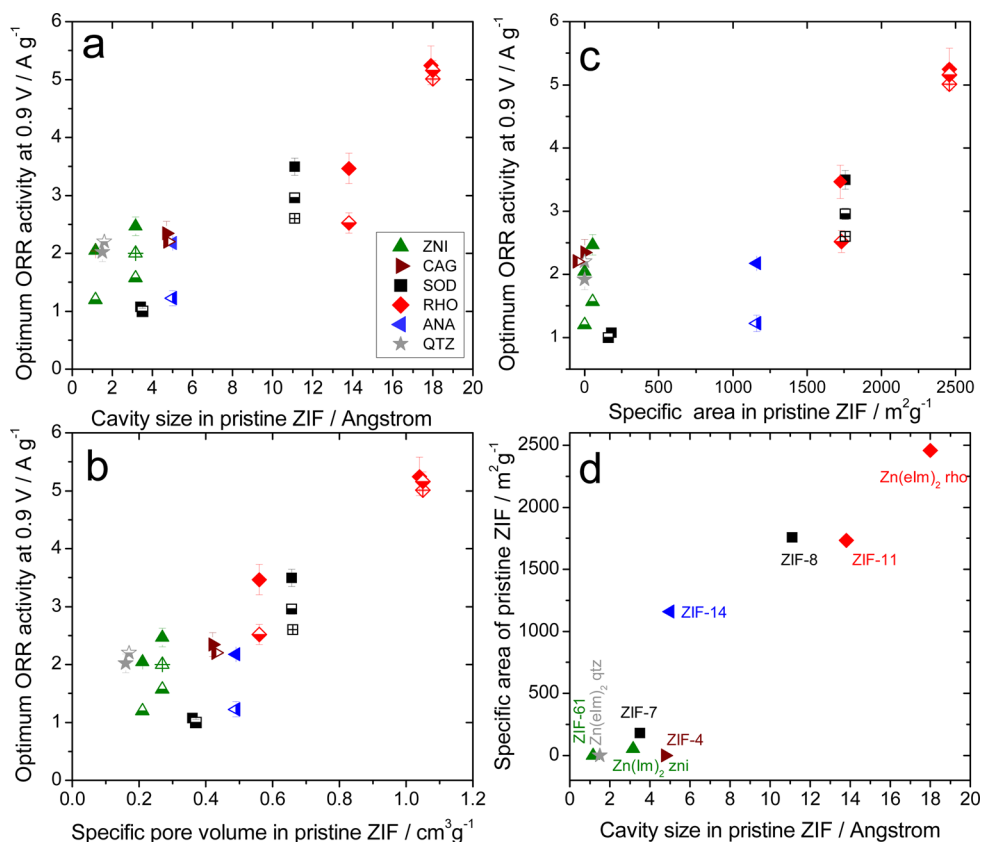
Figure 5. Correlation between optimum ORR activity of Fe−N−C catalysts and structural parameters of pristine ZIFs. (a) Optimum ORR activity vs cavity size in pristine ZIFs, (b) optimum ORR activity vs specific pore volume in pristine ZIFs, (c) optimum ORR activity vs specific area of pristine ZIFs, and (d) specific area of pristine ZIFs vs cavity size in pristine ZIFs. Activity measured for the first series of Fe−N−C catalysts (filled symbols), second series of catalysts (half-filled symbols), and catalysts prepared via one-pot approaches (open symbols with cross).

from ZIF-11. Further analysis shows that the amorphization extent is positively correlated with the cavity size of ZIFs or, expressed differently, with their specific pore volume. This is clearly highlighted in Figure 4a, with the XRD patterns arranged from top to bottom according to increasing cavity size in ZIF. These results are fully consistent with experimental and computational studies on the mechanical properties of ZIFs.[38,39] The elastic modulus and hardness of ZIFs have been shown to decrease with increasing mass-specific pore volume (Figure 14 in ref 38.). In particular, ZIF-7 and ZIF-4 are denser and thus harder materials than ZIF-8, in line with amorphization trends seen in Figure 4a. Compression-induced amorphization of MOFs and ZIFs is a topic of current research,[40−42] while ball-milling-induced amorphization has previously been reported for several ZIFs, in particular ZIF-8.[43,44] While the detailed organization of amorphized MOFs and ZIFs is still largely unexplored,[41] it has been shown that such materials either still display accessible internal porosity[42] or the internal porosity still exists but is no longer accessible by external molecular probes (most often N_2). The presence or absence of internal porosity can be revealed by helium pycnometry. Similar densities of 1.45 and 1.52 g cm^{-3} have been reported with this method for crystalline and fully amorphized nano-ZIF-8.[43] This shows that even amorphized (BET area of 56 m^2 g^{-1} instead of 1600 m^2 g^{-1} for crystalline ZIF-8, indicating that pores are inaccessible to N_2 after amorphization), ZIF-8 still possessed most of the internal cavities existing in crystalline ZIF-8, with these cavities being accessible to He.[43,44] The results suggest that amorphization

leads to a spatial reorganization of ligands, leading to shrunken apertures. The existence of cavities in amorphized ZIFs probably plays an important role toward the conversion of ZIFs into highly microporous carbons during pyrolysis.

While it seems reasonable to assume that the mass-specific volume of open and closed porosities in amorphized ZIFs scales with the open and closed porosities in crystalline ZIFs, justifying the attempts to draw correlations between ORR activity of Fe−N−C catalysts and structural features of crystalline ZIFs (Figure 3c,d), the amorphous character of ZIFs in this set of catalyst precursors however casts a doubt on the true meaning of such correlations. In order to prove or disprove the link between structure of pristine ZIFs and final ORR activities, it was necessary to design a second series of catalysts whose catalyst precursors retain the crystalline ZIF structures.

Structure−Activity Relationships for Catalysts Derived from Crystalline Precursors. In order to achieve this, the milling parameters (ball-to-powder mass ratio, milling speed, and milling duration) needed modification. To minimize changes in the milling procedure, we decided to investigate the effect of reduced milling speed. A range of milling speeds was first investigated on ZIF-8 that completely amorphized after milling at 400 rpm (Figure 4a). Figure S8 shows that the XRD pattern of ZIF-8 is unmodified after milling at 100 rpm and quasi-unmodified after milling at 200 rpm, while amorphization is significant after milling at 300 rpm. The milling speed of 100 rpm was thereafter selected to prepare another set of Fe−N−C catalysts from all nine ZIFs. It was verified that all catalyst

precursors retained the crystalline structure of their parent ZIF after milling ferrous acetate, phen and each ZIF at 100 rpm (Figure S9). Figure 4b highlights for selected ZIFs that the reduced milling speed was effective in avoiding the amorphization observed earlier after milling at 400 rpm.

This set of catalyst precursors prepared at 100 rpm milling speed was then pyrolyzed under the same conditions as those employed to synthesize the first set of Fe−N−C catalysts. A single pyrolysis temperature was applied to any catalyst precursor, selecting for each ZIF the pyrolysis temperature that led to the highest ORR activity within the first series of catalysts. If a memory effect from the pristine ZIF structures (such as retained mass-specific pore volume) played a role in setting the final ORR activity of Fe−N−C catalysts in the first series of catalysts, then the optimum pyrolysis temperature for each ZIF should remain the same for the second set of catalysts. The preliminary correlations observed in Figure 3 on the first series of catalysts were reproduced with the second series of catalysts (Figure 5). Figure 5a now proves without ambiguity the positive correlation between ORR activity of Fe−N−C catalysts and the cavity size in pristine ZIFs. Not only the trend but also the absolute ORR activity of Fe−N−C catalysts of the first series (filled symbols) and second series (half-filled symbols) of materials are very similar. It is particularly interesting to see that the three ZIF structures that had amorphized least during 400 rpm milling ($Zn(eIm)_2$ qtz, ZIF-7, and ZIF-4; see Figures 4 and S7) resulted in Fe−N−C catalysts with identical ORR activities after milling the catalyst precursors at either 100 or 400 rpm (Figure 5a, see the gray stars ($Zn(eIm)_2$ qtz), the black squares with cavity size 3.5 Å (ZIF-7), and the brown triangles (ZIF-4)). This supports the idea that structural properties of the pristine ZIFs play a key role in setting the final ORR activity of Fe−N−C catalysts. For other ZIFs, reduced milling speed from 400 to 100 rpm resulted in a slightly decreased ORR activity of the corresponding Fe−N−C catalysts (compare ZIF-by-ZIF the filled and half-filled symbols in Figure 5a). While no clear explanation for this slight impact can be given at this stage, several possible positive effects brought by higher milling speed may be mentioned, such as reduced average crystal size of ZIFs and modified thermal stabilities of an amorphized ZIF versus that of a crystalline ZIF. TGA indicated that amorphized ZIF-8 starts decomposing at 418 °C, compared to 486 °C for crystalline ZIF-8.[44] The other preliminary correlations observed on the first set of catalysts are also confirmed, namely, the positive correlation between ORR activity and specific pore volume in pristine ZIFs (Figure 5b) as well as the positive correlation between ORR activity and specific area in pristine ZIFs (Figure 5c). For ZIF materials, all three correlations are inter-related since cavity size, specific pore volume, and specific area all increase continuously from the less to the more open structures (Figure 5d).

Taken together, the results from both sets of catalysts identify a positive correlation between the cavity size (or specific pore volume) in pristine ZIFs and the final ORR activity of Fe−N−C catalysts; phen, and even more so the $Fe(phen)_3$ complex that might form even during dry milling, are too large to enter the internal porosity of pristine ZIFs and should thus have remained on the outer surface of the pristine or amorphized ZIF crystals. If structural parameters (cavity size, specific pore volume) of sacrificial ZIFs really underpin the ORR activity of Fe−N−C catalysts, then the location of Fe ions in the catalyst precursors should not much impact the final

ORR activity. In order to verify this, we synthesized additional catalyst precursors according to one-pot syntheses approaches, whereby the ligand, Zn(II) salt, Fe(II) salt, and phen are simultaneously present during ZIF crystallization.[13] While this approach conveniently results in the direct synthesis of an Fe−N−C catalyst precursor, alleviating the need for mixing by milling, the presence of Fe(II) salt or $Fe(phen)_3$ complex within the ZIF structures may however lead to modified XRD patterns relative to the targeted ZIF structures. This would imply novel but unknown structures, thereby impeding the identification of structure−property relationships. Various one-pot synthesis approaches were investigated for different ZIF structures examined in this work. However, only catalyst precursors having an XRD pattern matching that of a pure ZIF with known structure were retained for electrochemical evaluation. Catalyst precursors obtained via a one-pot approach and characterized by XRD patterns matching the $Zn(Im)_2$ zni, ZIF-8, and $Zn(eIm)_2$ rho structures were successfully prepared. After direct pyrolysis in NH_3 (no milling of catalyst precursors), the corresponding Fe−N−C catalysts were evaluated in a single-cell fixture. Their ORR activities proved to be very similar to those measured for catalysts obtained by milling at 100 or 400 rpm the corresponding ZIF with ferrous acetate and phen (see Figure 5a, open symbols with cross inside). These results further confirm that structural parameters of the pristine ZIFs are keys to the final ORR activity of Fe−N−C catalysts. The location of Fe(II) cations, outside or inside ZIF crystals, seems less important for the ORR activity of the final materials, as long as Fe(II) cations are well-dispersed in the catalyst precursors. As a whole, the results therefore demonstrate that increased cavity size and increased specific volume in ZIF structures helps directing their transformation into more active Fe−N−C catalysts.

Fe−N−C Structure to ORR Activity Relationships. While correlations between the structure of catalyst precursors based on sacrificial ZIFs and the ORR activity of Fe−N−C catalysts is of practical interest, it would also be of interest to understand which structural parameters of Fe−N−C catalysts prepared from different ZIFs were optimized with $Zn(eIm)_2$ rho. The two series of Fe−N−C catalysts were characterized by looking at the carbon structure of such materials. In order to prove or disprove a templating effect of the cavity size or specific area from the pristine ZIFs to the Fe−N−C materials, N_2 sorption measurements were measured on the first series of optimized Fe−N−C catalysts (Figure S10). Their sorption isotherms are characteristic of micro- and mesoporous materials, except for $Zn(eIm)_2$ qtz that hardly shows any microporosity but is characterized by large mesopores or macropores. Other materials show micropores with pore size <20 Å (N_2 volume adsorbed at $P/P^0 < 0.05$), small mesopores of 20−40 Å (hysteresis effect at $P/P^0 > 0.4$), and larger mesopores (amount proportional to the slope of the isotherm for $0.1 < P/P^0 < 0.8$). The fact that all Fe−N−C materials present some open porosity to the N_2 probe molecule while four pristine ZIFs are nonporous (see Table 1, ZIF-61, $Zn(eIm)_2$ qtz, $Zn(Im)_2$ zni and ZIF-4) is a first indication that the cavity existing in pristine ZIFs is not replicated in micropores of similar size in Fe−N−C catalysts. To better evidence this, the isotherms were analyzed with a sorption model based on quench solid density functional theory (see the Methods section). The resulting pore size distributions are shown in Figure 6a. Micropores with size in the range of 5−20 Å are evidenced, while small mesopores in the range 27−37 Å
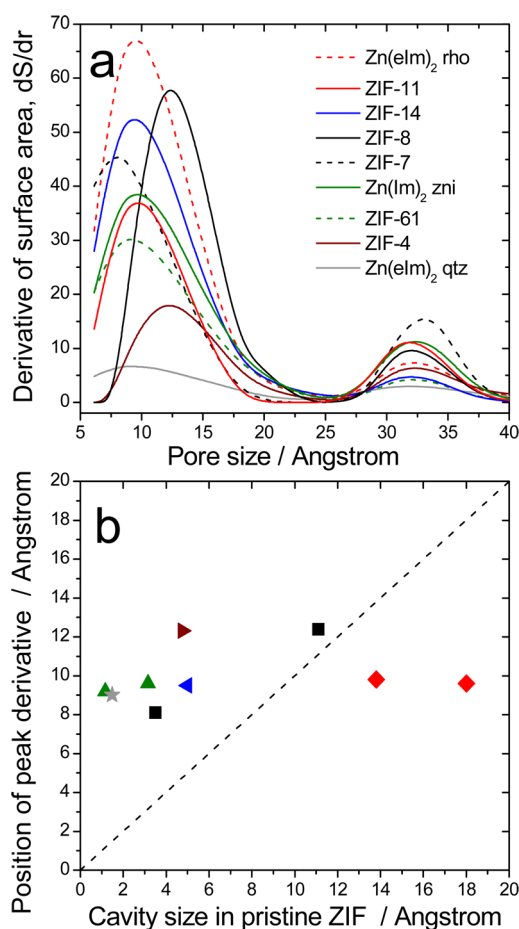
Figure 6. Characterization by N_2 sorption of the porous structure in the first series of Fe−N−C catalysts. (a) Derivative of specific surface area dS/dr as a function of pore size, as obtained via QSDFT analysis of the desorption branches of the isotherms; (b) pore size at which the derivative dS/dr is maximum in Fe−N−C catalysts as a function of the cavity size in pristine ZIFs.

are also observed. Since micropores are known to be important for Fe−N−C catalysts and in particular for NH_3-pyrolyzed Fe−N−C catalysts,[45,46] the average micropore size was estimated for each material with the pore size at which the derivative dS/dr is maximum. The comparison between the average micropore size in optimized Fe−N−C materials and the cavity size in the corresponding pristine ZIFs shows no correlation between these two structural parameters (Figure 6b). The

dashed line in Figure 6b highlights that ZIFs with a cavity size <7 Å resulted in Fe−N−C materials with an average micropore size larger than that in pristine ZIFs while ZIFs with a cavity size >12 Å resulted in Fe−N−C materials with an average micropore size smaller than that in pristine ZIFs. ZIF-8 stands at the crossroad of these trends, with nearly identical sizes for the cavity in the pristine ZIF and for the average micropore size in the resulting Fe−N−C catalyst. While all Fe−N−C materials have similar average micropore size (8.0−12.5 Å), the amounts of micropores vastly differ among the materials, as reflected by the large differences in microporous surface area and total specific area of the catalysts (Figure 6a and Table 2). A weak correlation between ORR activity and BET specific area of the first series of Fe−N−C catalysts is observed (Figure S11). This weak correlation between activity and surface area is not improved when considering only the microporous surface area (not shown). The BET area and microporous area of these materials are linearly inter-related (Figure S12). In summary, the pyrolysis of all ZIF materials resulted in similar average micropore sizes and pore size distributions in Fe−N−C materials. Consequently, the microporous ZIFs with highest specific pore volume also resulted in Fe−N−C catalysts with high BET surface area and high microporous specific area (ZIF-8, ZIF-11, and $Zn(eIm)_2$ rho). The BET surface area and microporous specific area of this series of catalysts are however not the sole factors determining the ORR activity, as shown by the moderate activity of the Fe−N−C catalyst derived from ZIF-14 in spite of high BET and microporous surface areas (Figure S11 and Table 2). While a high microporous specific area is a necessary condition for such materials in order to potentially host many FeN_4 moieties,[45] the ORR activity is *in fine* set by the formation of FeN_4 moieties. Iron supersaturation during pyrolysis may lead to the formation of inactive Fe crystalline structures instead of FeN_4 moieties. The dispersion of Fe might be favored with ZIFs having a high mass-specific pore volume, thereby minimizing the formation of metallic and metal−carbide iron structures during pyrolysis. Mössbauer spectroscopy was applied to investigate this. Figure S13 shows the Mössbauer spectra for four Fe−N−C catalysts of the second series of materials. The spectra of the optimized catalysts derived from $Zn(Im)_2$ zni and ZIF-7 could be fitted with a major fraction of spectral components assigned to crystalline Fe structures (α-Fe and iron carbide (Fe_xC) sextets, singlet of γ-Fe, gray doublet assigned to Fe nitride crystalline particles (Fe_xN)) and a minor fraction of doublets D1 and D2 assigned to ORR-active FeN_4 moieties in low- and medium-spin states.[12,18,31] The sum D1 + D2 represents only 5.2% of

Table 2. Specific Areas for Optimized Catalysts of the First Series of Fe−N−C Materials[a]

ZIF structure from which the Fe−N−C catalyst was derived	ZIF topology	specific surface area of catalyst ($m^2\ g^{-1}$)	microporous surface area of catalyst ($m^2\ g^{-1}$)	mesoporous surface area of catalyst ($m^2\ g^{-1}$)
$Zn(Im)$ (mIm), ZIF-61	zni	403	285	26
$Zn(eIm)_2$	qtz	172	68	46
$Zn(Im)_2$	zni	554	350	54
$Zn(bzIm)_2$, ZIF-7	sod	528	366	49
$Zn(Im)_2$, ZIF-4	cag	322	138	50
$Zn(eIm)_2$, ZIF-14	ana	620	471	30
$Zn(mIm)_2$, ZIF-8	sod	728	393	40
$Zn(bzIm)_2$, ZIF-11	rho	421	272	38
$Zn(eIm)_2$	rho	799	544	53

[a]The total specific area was estimated from BET analysis, while the microporous and mesoporous areas were obtained from the analysis of the desorption isotherms with the quench solid density functional theory.

the total absorption area for the catalyst derived from $Zn(Im)_2$ and 17.6% for that derived from ZIF-7 (Table S2). The analysis of the spectra of the catalysts derived from ZIF-8 and $Zn(eIm)_2$ rho reveals a higher fraction of the area summed for doublets D1 and D2, 17.8 and 42.1% of the total absorption area, respectively, for the two catalysts. The $Zn(eIm)_2$ rho catalyst is in particular the only one showing an ORR activity significantly higher than that of the ZIF-8 derived catalyst (Figure 5). The broad singlet in the spectrum of that catalyst has previously been observed on some Fe−N−C catalysts and is assigned to (sub-)nanometric iron nitride crystallites, in line with the average high dispersion of Fe in that catalyst. Mössbauer characterization thus indicates that the fraction of Fe that transformed into ORR-active FeN_4 moieties during pyrolysis is generally higher for catalyst precursors based on ZIF with large cavity size, or large specific volume, than that for catalyst precursors based on ZIFs with small cavity size or small specific pore volume. This interpretation is further supported by the mass activity at 0.9 V of ca. 1 A g^{-1} measured by us for a catalyst prepared via direct NH_3 pyrolysis of commercial ZIF-8 (Basolite Z1200), without adding iron. This is in line with a recent report from Dodelet's group (Figure 9 in ref 47). This activity corresponds to the lower-end activity range measured for the present Fe−N−C materials comprising a very low fraction of Fe as FeN_4 moieties (e.g., those derived from ZIF-7 or $Zn(Im)_2$ zni, Figure S13). The ORR activity for Basolite Z1200 pyrolyzed alone in NH_3 either stems from an intrinsic ORR activity of surface nitrogen groups or from trace amounts of FeN_4 sites, with iron being present at trace level in Basolite Z1200. Its Fe content was estimated from inductively coupled spectrometry and X-ray absorption spectroscopy to be in the range of 0.01−0.03 wt % Fe.

In addition to improved Fe dispersion, the large cavity size and large pore apertures of ZIFs having a high specific pore volume are also efficient for quickly removing the volatile products formed from the decomposition of ZIFs during pyrolysis. This is particularly important when applying a flash pyrolysis (see Methods and Supporting Information in ref 45) with high rates of formation of associated volatile products, where all ZIF materials lose 85−95% of their initial mass after 15 min of pyrolysis; most of this mass loss probably occurring in the first tens of seconds of the pyrolysis. It is noted that an accurate and reproducible control of pyrolysis temperature and duration as well as introduction method of the catalyst precursor into the oven is important to reach reproducible results with the flash pyrolysis method (see ref 45 for detailed Methods and Supporting Iinformation for flash pyrolysis used in the present work).

CONCLUSION

This work sheds light on the importance of the structure of sacrificial ZIFs employed for the preparation of Fe−N−C catalysts with high ORR activity. In particular, the cavity size and specific pore volume of pristine ZIFs are crucial for directing the transformation during flash pyrolysis of the iron, nitrogen, and carbon precursors toward the formation of FeN_4 moieties, the most active sites for ORR in acidic medium. The identification of these structure−property relationships will help in selecting or designing novel MOFs, potentially leading to even more active Fe−N−C catalysts. The concept of high specific pore volume may also be important for porous organic polymers used as sacrificial precursors. The outcome of the present study may also be viewed as a particular case of an even

more general concept whereby the high dispersion of Fe atoms in the catalyst precursor combined with the efficient removal of volatile species formed during the heating of sacrificial (metal−)organic materials are keys to the synthesis of Fe−N−C materials with a high content of ORR-active FeN_4 moieties and an open structure. While slower pyrolysis modes (ramp mode) decrease the rate of volatile product formation and may help the transformation of ZIFs into open carbon structures,[36] the improved spatial dispersion of Fe in catalyst precursors comprising ZIFs with a high specific pore volume is also expected to be advantageous when applying pyrolyses procedures slower than the presently investigated flash mode.

Beyond ORR activity, the performance of Fe−N−C cathodes in a fuel cell is also controlled by the macroscopic morphology of Fe−N−C materials. The latter is strongly influenced by the crystal size of the pristine MOFs, with templating effects from MOF crystals to carbon particles being already demonstrated.[36,48,49] Combined large cavity size and appropriate crystal size of sacrificial MOFs will thus be necessary for improved power performance of Fe−N−C cathodes. Significant efforts in synthesis are needed to control both the micro- and macrostructure of porous MOFs, with synthesis methods amenable to scaled-up production.

METHODS

ZIF Synthesis. ZIF-8 was purchased from Sigma-Aldrich under the trade name Basolite Z1200. All other materials were synthesized according to published procedures, as detailed briefly below. ZIF-61, ZIF-4, and ZIF-14 were synthesized according to Banerjee et al.[35] $Zn(eIm)_2$ qtz, $Zn(eIm)_2$ rho, and $Zn(Im)_2$ zni were prepared according to Beldon et al.[50]

ZIF-61. $Zn(NO_3)_2$ (13 mL, 0.15 M in *N,N*-dimethylformamide (DMF) solution, 1.9 mmol), Im (26 mL, 0.15 M DMF solution, 3.9 mmol), and mIm (26 mL, 0.15 M in DMF solution, 3.9 mmol) were placed in a 125 mL Parr vessel. The reaction was heated to 100 °C for 96 h leading to the formation of a white precipitate. The solid was isolated by vacuum filtration, washed with DMF, and left to dry in the air.

ZIF-4. $Zn(NO_3)_2$ (53 mL, 0.15 M in DMF solution, 7.9 mmol) and Im (16 mL, 0.15 M in DMF solution, 2.4 mmol) were placed in a 125 mL Parr autoclave vessel. The reaction was heated to 100 °C for 72 h leading to the formation of a white precipitate which was isolated by vacuum filtration. The material was washed with DMF and then left to dry in the air.

ZIF-14. $Zn(NO_3)_2$ (18 mL, 0.2 M in DMF solution, 3.6 mmol) and eIm (47 mL, 0.2 M in DMF solution, 9.6 mmol) were placed in a 125 mL Parr reaction vessel which was sealed and heated to 85 °C for 100 h leading to the formation of a white precipitate. The solid was isolated by vacuum filtration, washed with DMF, and left to dry in the air.

Zn(eIm)₂ qtz. ZnO (8.2014 g, 101 mmol) and eIm (20.1416 g, 210 mmol) were placed in a zirconium mill pot with DMF (2 mL), ammonium nitrate (0.1 g, 1.3 mmol), and zirconia milling balls. The mixture was ground for 60 min in a Fritsch mill at 400 rpm. The white solid obtained was washed with DMF and dried in air.

Zn(eIm)₂ rho. ZnO (8.2014 g, 101 mmol) and eIm (20.1416 g, 210 mmol) were placed in a zirconium mill pot with with DMF (2 mL), ammonium sulfate (0.1 g, 0.7 mmol), and zirconia milling balls. The mixture was ground for 30 min in a Fritsch mill at 400 rpm. The white solid obtained was washed with DMF and dried in air.

Zn(Im)₂ zni. ZnO (8.2471 g, 101 mmol), Im (14.5078 g, 213 mmol), and ammonium nitrate (0.1 g, 1.3 mmol) were placed in a zirconium mill pot with zirconia milling balls. The mixture was ground in the planetary mill at 400 rpm for 30 min. The white solid obtained was washed with DMF and dried in air.

ZIF-7. This material was prepared according to Park et al.[34] $Zn(NO_3)_2$ (0.8015 g, 2.6 mmol) and bIm (0.2328 g, 1.9 mmol) were

dissolved in DMF (70 mL). The reaction was heated to 130 °C for 48 h leading to the formation of a white precipitate. The solid was isolated by vacuum filtration, washed with DMF, and left to dry in the air.

ZIF-11. This material was prepared according to He et al.[51] bIm (15.2 g, 128.8 mmol) was dissolved in a mixture of MeOH (900 mL) and toluene (600 mL). Ammonium hydroxide (35% by wt, 14.2 mL, 128.8 mmol) was then added. While the resulting solution was stirred, zinc acetate (11.8 g, 64.4 mmol) was added; the mixture was left to stir at room temperature for a further 3 h. The product was isolated by vacuum filtration and washed in ethanol three times before being dried in air to afford a white powder.

One-Pot Syntheses. One-pot materials involving ZIF-8 and $Zn(Im)_2$-zni were prepared according to Zhao et al.[13]

$Zn(eIm)_2$ rho: ZnO (3.0047 g, 37 mmol), eIm (7.1495 g, 72 mmol), $(NH_4)_2SO_4$ (0.7541 g, 7 mmol), $Fe(OAc)_2$ (0.1188 g, 0.68 mmol), and 1,10-phenanthroline (2.377 g, 13 mmol) were placed in a zirconium mill pot with DMF (6 mL) and zirconia milling balls. The mixture was ground for 30 min in a Fritsch mill at 400 rpm. The light pink solid obtained was dried in air.

ZIF-8: ZnO (2.2803 g, 28 mmol), mIm (5.0349 g, 61 mmol), $Fe(OAc)_2$ (0.0679 g), and 1,10-phenanthroline (1.2092 g, 6.7 mmol) were ground into a homogeneous mixture then sealed in solvothermal bomb under Ar. The reaction mixture was heated to 180 °C for 18 h. Upon cooling a damp red solid was obtained. The product was dried under vacuum at 100 °C for 3 h and a pink solid product obtained.

$Zn(Im)_2$ zni: ZnO (2.2709 g, 28 mmol), Im (4.1942 g, 62 mmol), $Fe(OAc)_2$ (0.0655 g, 0.35 mmol), and 1,10-phenanthroline (1.2330 g, 6.9 mmol) were ground into a homogeneous mixture then sealed in solvothermal bomb under Ar. The reaction mixture was heated to 180 °C for 18 h and a pink solid product obtained.

Simulation-Assisted Structural Determination of ZIF Materials. The initial atomic coordinates of the ZIF frameworks were first taken from the refined structures obtained by XRD already published.[32,34,52] All these models were then energy-minimized in the space group determined experimentally by keeping the cell parameters fixed. The optimized structures corresponding to the lowest energy for each modified form was then selected. The universal force field (UFF,[53]) for the Lennard-Jones parameters and the charges calculated from the qeq method,[54] as implemented in the Materials Studio software (version 5.0, Accelrys Inc., San Diego, USA), were considered to model the interactions between the whole systems. Such a strategy based on the UFF force field has previously been successfully employed to construct plausible structure of various MOFs known as "Matériaux Institut Lavoisier" (MIL) MILs including the MIL-88(Fe) and MIL-53(Fe) series as well as different forms of Co(BDP).[55–57] The Ewald summation was considered for calculating the electrostatic interactions while the short-range interactions were evaluated using a cutoff distance of 12 Å. The convergence criteria were set to 1.0×10^{-5} kcal mol^{-1}, 0.001 kcal mol^{-1} Å^{-1}, and 1.0×10^{-5} Å for energy, force, and displacement, respectively. The plausible theoretical structure was determined by the energy criteria. All geometry optimizations converged to provide the crystallographic structure for each ZIF structure with the imposed symmetry. The comparison between experimental and theoretical diffractograms calculated from the thus-obtained plausible structures enabled us to identify the structure of the synthesized materials.

Determination of Specific Area, Pore Volume, and Pore Size Distribution from ZIF Structures. The accessible surface area of the simulated ZIF structures was estimated using the strategy previously reported by Düren et al.[58] This surface was calculated from the center of a nitrogen probe molecule rolling across the surface. While the diameter of the nitrogen probe molecule was considered to be 3.681 Å (radius 1.84 Å), the diameters of each atom constituting the ZIF structures were taken from the UFF force field.[53] Complementary calculations have been performed using a smaller probe (diameter 2.8 Å) as proposed by Park et al.[34] This smaller radius has been shown to better correspond to the experimental BET surface areas obtained for some MOFs, probably because of the flexibility of some MOF structures. The mass-specific free volume was calculated for each simulated structure by using a similar method of trial insertions within the entire volume of the unit cell. A probe size of 0 Å was used to enable us determining the total free volume of the unit cell that is not occupied by the atoms of the framework.[58] The free volume calculated in this way was verified to be very similar to the free volume that can be deduced from experimental N_2 sorption isotherms. The plateau observed in sorption isotherms corresponds to the filling of microporous voids by liquid N_2, allowing the back-calculation of mass-specific free volume for microporous MOF powders. Using the same parametrization for the framework (UFF), the methodology of Gelb and Gubbins was used to calculate the pore size distribution.[59] From the pore size distribution function, it is possible to estimate the cavity size as well as the size of the windows allowing passing from one cavity to another (aperture). Generally, the aperture is smaller than the cages, and the distinction of the pore size for aperture or cavity is performed using the structure.

Catalyst Synthesis. Except for one-pot materials, all catalyst precursors were prepared from a given ZIF, Fe(II) acetate, and phen. Weighed amounts of the powders of Fe salt, phen, and ZIF (31.45, 200, and 800 mg, respectively), all previously dried overnight at 80 °C, were poured into a ZrO_2 crucible (45 mL). Then, 100 zirconium oxide balls of 5 mm diameter were added, and the crucible was sealed under air and placed in a planetary ball-miller (FRITSCH Pulverisette 7 Premium) to undergo 4 cycles of 30 min of ball-milling at either 400 rpm milling speed (first series of catalysts) or 100 rpm (second series of catalysts). The resulting catalyst precursor was pyrolyzed for 15 min in flowing NH_3 at 900, 950, 1000, or 1050 °C. One-pot materials were not subjected to milling and were pyrolyzed with the same procedure. The split-hinge oven and quartz tube were equilibrated at the set temperature for 2 h before pushing the quartz boat and catalyst precursor powder into the center of the heating zone with an external magnet, within 1.0–1.5 min.[45] The quartz boat and catalyst then remained for 15 min in the oven, and the pyrolysis was terminated by opening the split-hinge oven and removing the quartz tube. The catalyst powder was collected and gently ground with a marble mortar and pestle. No other post-treatment was applied to the catalysts.

Membrane Electrode Assembly Preparation and Fuel Cell Measurement. Cathode inks were prepared using the following formulation: 20 mg of catalyst, 652 μL of 5 wt % Nafion solution containing 15–20% water, 326 μL of ethanol, and 272 μL of deionized water. The ink was alternatively sonicated and agitated with a vortex mixer every 15 min, for a total of 1 h. Then, a 303 μL aliquot of the catalyst ink was deposited on the microporous layer of an uncatalysed 4.84 cm^2 gas diffusion layer (Sigracet S10-BC) to reach a cathode catalyst loading of 1 mg cm^{-2}. The cathode was then placed in a vacuum oven at 90 °C to dry for 2 h. The anode used for all PEMFC characterizations performed in this work was 0.5 mg$_{Pt}$·cm^{-2} on Sigracet S10-BC. MEAs were prepared by hot-pressing 4.84 cm^2 anode and cathode against either side of a Nafion N117 membrane at 135 °C for 2 min. Current–voltage curves were recorded with a single-cell fuel cell with serpentine flow field (Fuel Cell Technologies Inc.) using an in-house fuel cell bench and a Biologic Potentiostat with a 50 A load and EC-Lab software. To record the polarization curves, the fuel cell temperature was 80 °C, the humidifiers were set at 100 °C, and the inlet gas pressures were set to 1 bar gauge for both anode and cathode sides. The flow rates for humidified H_2 and O_2 were ca. 50–70 sccm downstream of the fuel cell. Polarization curves were recorded by scanning the cell voltage at 0.5 mV·s^{-1}. The cell resistance was measured with electrochemical impedance spectroscopy, by reading the high-frequency intercept with x-axis in a Nyquist plot.

X-ray Diffraction, Porosimetry, and Scanning Electron Microscopy. X-ray diffraction was conducted using a PANanalytical X'Pert Pro powder X-ray diffractometer. N_2 sorption analysis was performed at liquid nitrogen temperature (77 K) with a Micromeritics ASAP 2020 instrument. Prior to the measurements, Fe–N–C materials were outgassed at 200 °C for 5 h in flowing nitrogen to remove guest molecules or moisture. The pore size distribution of Fe–N–C materials was calculated by fitting the full isotherm with the quench solid density functional theory model with slit pore geometry from NovaWin (Quantachrome Instruments). SEM micrographs were obtained with a Hitachi S-4800 apparatus after gold metallization.

ASSOCIATED CONTENT

S Supporting Information

The Supporting Information is available free of charge on the ACS Publications website at DOI: 10.1021/jacs.6b11248.

> XRD of ZIF and Fe−N−C materials, calculated pore size distribution of ZIFs, experimental pore size distribution of Fe−N−C materials, SEM images of ZIF and Fe−N−C materials, N_2 sorption isotherms of Fe−N−C materials, and Mössbauer spectra of Fe−N−C materials (PDF)

AUTHOR INFORMATION

Corresponding Author

*E-mail: frederic.jaouen@umontpellier.fr. Tel.: + 33 4 67 14 32 11.

ORCID

Frédéric Jaouen: 0000-0001-9836-3261

Present Address

V.A.: Commissariat à l'Energie Atomique - LETI, Campus Minatec, Grenoble CEDEX 38000, France. E-mail: Marie-JosepheVanessa.ARMEL@cea.fr.

Notes

The authors declare the following competing financial interest(s): A patent application related to this work has been filed.

REFERENCES

(1) Wagner, F. T.; Lakshmanan, B.; Mathias, M. F. *J. Phys. Chem. Lett.* **2010**, *1*, 2204−2219.
(2) Thomas, C. E. *Int. J. Hydrogen Energy* **2009**, *34*, 6005−6020.
(3) Debe, M. *Nature* **2012**, *486*, 43−51.
(4) Chen, C.; Kang, Y.; Huo, Z.; Zhu, Z.; Huang, W.; Xin, H. L.; Snyder, J. D.; Li, D.; Herron, J. A.; Mavrikakis, M.; Chi, M.; More, K. L.; Li, Y.; Markovic, N. M.; Somorjai, G. A.; Yang, P.; Stamenkovic, V. R. *Science* **2014**, *343*, 1339−1343.
(5) Wang, C.; Markovic, N. M.; Stamenkovic, V. R. *ACS Catal.* **2012**, *2*, 891−898.
(6) Strasser, P.; Koh, S.; Anniyev, T.; Greeley, J.; More, K.; Yu, C.; Liu, Z.; Kaya, S.; Nordlund, D.; Ogasawara, H.; Toney, M. F.; Nilsson, A. *Nat. Chem.* **2010**, *2*, 454−460.
(7) Proietti, E.; Jaouen, F.; Lefèvre, M.; Larouche, N.; Tian, J.; Herranz, J.; Dodelet, J. P. *Nat. Commun.* **2011**, *2*, 416.
(8) Wu, G.; More, K. L.; Johnston, C. M.; Zelenay, P. *Science* **2011**, *332*, 443−447.
(9) Wu, G.; Zelenay, P. *Acc. Chem. Res.* **2013**, *46*, 1878−1889.
(10) Shui, J.; Chen, C.; Grabstanowicz, L.; Zhao, D.; Liu, D. J. *Proc. Natl. Acad. Sci. U. S. A.* **2015**, *112*, 10629−10634.
(11) Barkholtz, H. M.; Chong, L.; Kaiser, Z. B.; Xu, T.; Liu, D. J. *Catalysts* **2015**, *5*, 955−965.
(12) Tian, J.; Morozan, A.; Sougrati, M. T.; Lefèvre, M.; Chenitz, R.; Dodelet, J. P.; Jones, D.; Jaouen, F. *Angew. Chem., Int. Ed.* **2013**, *52*, 6867−6870.
(13) Zhao, D.; Shui, J.-L.; Grabstanowicz, L. R.; Chen, C.; Commet, S. M.; Xu, T.; Lu, J.; Liu, D. J. *Adv. Mater.* **2014**, *26*, 1093−1097.
(14) Strickland, K.; Miner, E.; Jia, Q.; Tylus, U.; Ramaswamy, N.; Liang, W.; Sougrati, M.-T.; Jaouen, F.; Mukerjee, S. *Nat. Commun.* **2015**, *6*, 7343.
(15) Ma, S.; Goenaga, G. A.; Call, A. V.; Liu, D. J. *Chem. - Eur. J.* **2011**, *17*, 2063−2067.
(16) Lefèvre, M.; Dodelet, J. P. *ECS Trans.* **2012**, *45*, 35−44.
(17) Zhao, D.; Shui, J. L.; Chen, C.; Chen, X.; Reprogle, B. M.; Wang, D.; Liu, D. J. *Chem. Sci.* **2012**, *3*, 3200−3205.
(18) Kramm, U. I.; Herrmann-Geppert, I.; Fiechter, S.; Zehl, G.; Zizak, I.; Dorbandt, I.; Schmeisser, D.; Bogdanoff, P. *J. Mater. Chem. A* **2014**, *2*, 2663−2670.
(19) Jaouen, F.; Dodelet, J. P. *Electrochim. Acta* **2007**, *52*, 5975−5984.
(20) Wu, G.; Johnston, C. M.; Mack, N. H.; Artyushkova, K.; Ferrandon, M.; Nelson, M.; Lezama-Pacheco, J. S.; Conradson, S. D.; More, K. L.; Myers, D. L.; Zelenay, P. *J. Mater. Chem.* **2011**, *21*, 11392−11405.
(21) Wu, J.; Song, Y.; Zhou, R.; Chen, S.; Zuo, L.; Hou, H.; Wang, L. *J. Mater. Chem. A* **2015**, *3*, 7793−7798.
(22) Shang, L.; Yu, H.; Huang, X.; Bian, T.; Shi, R.; Zhao, Y.; Waterhouse, G.; Wu, L.-Z.; Tung, C.-H.; Zhang, T. *Adv. Mater.* **2016**, *28*, 1668−1674.
(23) Su, P.; Xiao, H.; Zhao, J.; Yao, Y.; Shao, Z.; Li, C.; Yang, Q. *Chem. Sci.* **2013**, *4*, 2941−2946.
(24) Tang, J.; Salunkhe, R. R.; Liu, J.; Torad, N. L.; Imura, M.; Furukawa, S.; Yamauchi, Y. *J. Am. Chem. Soc.* **2015**, *137*, 1572−1580.
(25) Li, Q.; Xu, P.; Gao, W.; Ma, S.; Zhang, G.; Cao, R.; Cho, J.; Wang, H.-L.; Wu, G. *Adv. Mater.* **2014**, *26*, 1378−1386.
(26) Palaniselvam, T.; Biswal, B. P.; Banerjee, R.; Kurungot, S. *Chem. - Eur. J.* **2013**, *19*, 9335−9342.
(27) Yuan, S.; Shui, J.-L.; Grabstanowicz, L.; Chen, C.; Commet, S.; Reprogle, B.; Xu, T.; Yu, L.; Liu, D. J. *Angew. Chem., Int. Ed.* **2013**, *52*, 8349−8353.
(28) Pachfule, P.; Biswal, B. P.; Banerjee, R. *Chem. - Eur. J.* **2012**, *18*, 11399−11408.
(29) Lim, S.; Suh, K.; Kim, Y.; Yoon, M.; Park, H.; Dybtsev, D. N.; Kim, K. *Chem. Commun.* **2012**, *48*, 7447−7449.
(30) Aiyappa, H. B.; Pachfule, P.; Banerjee, R.; Kurungot, S. *Cryst. Growth Des.* **2013**, *13*, 4195−4199.
(31) Zitolo, A.; Goellner, V.; Armel, V.; Sougrati, M.-T.; Mineva, T.; Stievano, L.; Fonda, E.; Jaouen, F. *Nat. Mater.* **2015**, *14*, 937−942.
(32) Phan, A.; Doonan, C. J.; Uribe-Romo, F. J.; Knobler, C. B.; O'Keeffe, M.; Yaghi, O. M. *Acc. Chem. Res.* **2010**, *43*, 58−67.
(33) Huang, X.; Zhang, J.; Chen, X. *Chin. Sci. Bull.* **2003**, *48*, 1531−1534.
(34) Park, K. S.; Ni, Z.; Côté, A. P.; Choi, J. Y.; Huang, R.; Uribe-Romo, F. J.; Chae, H. K.; O'Keeffe, M.; Yaghi, O. *Proc. Natl. Acad. Sci. U. S. A.* **2006**, *103*, 10186−10191.
(35) Banerjee, R.; Phan, A.; Wang, B.; Knobler, C.; Furukawa, H.; O'Keeffe, M.; Yaghi, O. M. *Science* **2008**, *319*, 939−943.
(36) Armel, V.; Hannauer, J.; Jaouen, F. *Catalysts* **2015**, *5*, 1333−1351.
(37) Manoj, B.; Kunjomana, A. G. *Int. J. Electrochem. Science* **2012**, *7*, 3127−3134.
(38) Tan, J. C.; Cheetham, A. K. *Chem. Soc. Rev.* **2011**, *40*, 1059−1080.
(39) Coudert, F.-X. *Chem. Mater.* **2015**, *27*, 1905−1916.
(40) Ortiz, A. U.; Boutin, A.; Fuchs, A. H.; Coudert, F.-X. *J. Phys. Chem. Lett.* **2013**, *4*, 1861−1865.
(41) Bennett, T. D.; Cheetham, A. K. *Acc. Chem. Res.* **2014**, *47*, 1555−1562.
(42) Chapman, K. W.; Halder, G. J.; Chupas, P. J. *J. Am. Chem. Soc.* **2009**, *131*, 17546−17547.

(43) Bennett, T. D.; Cao, S.; Tan, J. C.; Keen, D. A.; Bithell, E. G.; Beldon, P. J.; Friscic, T.; Cheetham, A. K. *J. Am. Chem. Soc.* **2011**, *133*, 14546−14549.

(44) Cao, S.; Bennett, T. D.; Keen, D. A.; Goodwin, A. L.; Cheetham, A. K. *Chem. Commun.* **2012**, *48*, 7805−7807.

(45) Jaouen, F.; Lefèvre, M.; Dodelet, J. P.; Cai, M. *J. Phys. Chem. B* **2006**, *110*, 5553−5558.

(46) Lefèvre, M.; Proietti, E.; Jaouen, F.; Dodelet, J. P. *Science* **2009**, *324*, 71−74.

(47) Zhang, G.; Chenitz, R.; Lefèvre, M.; Sun, S.; Dodelet, J.-P. *Nano Energy* **2016**, *29*, 111.

(48) Xia, W.; Zhu, J.; Guo, W.; An, L.; Xia, D.; Zou, R. *J. Mater. Chem. A* **2014**, *2*, 11606−11613.

(49) Zhang, L.; Su, Z.; Jiang, F.; Yang, L.; Qian, J.; Zhou, Y.; Li, W.; Hong, M. *Nanoscale* **2014**, *6*, 6590−6602.

(50) Beldon, P. J.; Fabian, L.; Stein, R. S.; Thirumurugan, A.; Cheetham, A. K.; Friscic, T. *Angew. Chem., Int. Ed.* **2010**, *49*, 9640−9643.

(51) He, M.; Yao, J.; Liu, Q.; Zhong, Z.; Wang, H. *Dalton Trans.* **2013**, *42*, 16608−16613.

(52) Dybtsev, D. N.; Chun, H.; Kim, K. *Angew. Chem., Int. Ed.* **2004**, *43*, 5033−5036.

(53) Rappé, A. K.; Casewit, C. J.; Colwell, K. S.; Goddard, W. A.; Skiff, W. M. *J. Am. Chem. Soc.* **1992**, *114*, 10024−10035.

(54) Rappé, A. K.; Goddard, W. A. *J. Phys. Chem.* **1991**, *95*, 3358−3363.

(55) Horcajada, P.; Salles, F.; Wuttke, Z.; Devic, T.; Heurtaux, D.; Maurin, G.; Vimont, A.; Daturi, M.; David, O.; Magnier, E.; Stock, N.; Filinchuk, Y.; Popov, D.; Riekel, C.; Férey, G.; Serre, C. *J. Am. Chem. Soc.* **2011**, *133*, 17839−17847.

(56) Devic, T.; Horcajada, P.; Serre, C.; Salles, F.; Maurin, G.; Moulin, B.; Heurtaux, D.; Clet, G.; Vimont, A.; Grenèche, J.-M.; Le Ouay, B.; Moreau, F.; Magnier, E.; Filinchuk, Y.; Marrot, J.; Lavalley, J.-C.; Daturi, M.; Férey, G. *J. Am. Chem. Soc.* **2010**, *132*, 1127−1136.

(57) Salles, F.; Maurin, G.; Serre, C.; Llewellyn, P. L.; Knöfel, C.; Choi, H. J.; Filinchuk, Y.; Oliviero, L.; Vimont, A.; Long, J. R.; Férey, G. *J. Am. Chem. Soc.* **2010**, *132*, 13782−13788.

(58) Düren, T.; Millange, F.; Férey, G.; Walton, K. S.; Snurr, R. Q. *J. Phys. Chem. C* **2007**, *111*, 15350−15356.

(59) Gelb, L. D.; Gubbins, K. E. *Langmuir* **1999**, *15*, 305−308.